



**HAL**  
open science

# Influence of porosity network on the chemo-mechanical evolution of low-pH cementitious materials subjected to calcareous attack

Mejdi Neji, Charlotte Dewitte, Benoît Durville

## ► To cite this version:

Mejdi Neji, Charlotte Dewitte, Benoît Durville. Influence of porosity network on the chemo-mechanical evolution of low-pH cementitious materials subjected to calcareous attack. *Construction and Building Materials*, 2023, 405, pp.133313. 10.1016/j.conbuildmat.2023.133313 . hal-04313331

**HAL Id: hal-04313331**

**<https://hal.science/hal-04313331>**

Submitted on 29 Nov 2023

**HAL** is a multi-disciplinary open access archive for the deposit and dissemination of scientific research documents, whether they are published or not. The documents may come from teaching and research institutions in France or abroad, or from public or private research centers.

L'archive ouverte pluridisciplinaire **HAL**, est destinée au dépôt et à la diffusion de documents scientifiques de niveau recherche, publiés ou non, émanant des établissements d'enseignement et de recherche français ou étrangers, des laboratoires publics ou privés.



Distributed under a Creative Commons Attribution - NonCommercial - NoDerivatives 4.0 International License

# Influence of porosity network on the chemo-mechanical evolution of low-pH cementitious materials subjected to calcareous attack.

M. Neji (1), C. Dewitte (1,3), B. Durville (2).

<sup>1</sup> Institute for Radiation Protection and Nuclear Safety (IRSN)/PSE-ENV/SEDRE/LETIS, BP 17, 92262 Fontenay-aux-Roses cedex, France

<sup>2</sup> Institute for Radiation Protection and Nuclear Safety (IRSN), /PSN-RES/SEREX/L2EC, 13115 Saint-Paul-Lez-Durance Cedex, France

<sup>3</sup> Université de Toulouse, UPS, INSA, LMDC (Laboratoire Matériaux et Durabilité des Constructions), 135 Avenue de Rangueil, 31077 Toulouse Cedex 04, France

---

## ABSTRACT

---

This paper presents a study which aims to understand the degradation mechanisms induced in a low-pH cementitious matrix by a calcareous attack and then, to evaluate the porosity network influence on the degradation scenario. To reach these goals, three experimental campaigns were carried out in parallel. Hardened low-pH cement paste samples were made in laboratory-controlled conditions, then immersed in calcareous water containing a small amount of water. Concrete samples were then cast in industrial conditions, cured in a controlled environment, then immersed in the same experimental device. Finally, massive concrete blocks were cast and cured outside with industrial processes before immersion in the attack water. Chemo-mechanical characterizations (SEM,  $\mu$ CT, micro/nano-indentation) were performed to estimate the degradation state of the samples. Geochemical modelling was performed to validate experimental observations. Calcium and magnesium enrichment are the main phenomena in all cases. However, the degradation scenario changes with the curing protocol. Porosity closing is observed in samples cured in a controlled environment, whereas industrial curing conditions induce non-negligible chemical alteration due to a skin effect.

---

**Highlights:** Low pH binder, Cement paste, Chemical degradation, Diffusion, Microstructure, Ground water.

## 1. Introduction

The French geological disposal project (CIGEO) for Intermediate Long-Lived Wastes (ILLW) and High-Level Wastes (HLW) features a facility in a clay rock formation to contain radionuclides and protect human habitation and its environment. In the ILLW plan, the cells are assumed to be composed of cementitious materials (liner, confinement plugs and waste containers), while all the sealing zones (horizontal and vertical) will consist of a bentonite plug placed between two concrete barriers, exposed to different kinds of natural waters (calcareous or clayey water) depending on the location in the facility.

To limit the interaction between concrete and host rock, cementitious formulations called "low-pH" have been designed internationally, composed of Portland cement mixed with pozzolanic additions. These additions to the clinker provide a Portlandite-free cementitious matrix, which reduces the pH of the interstitial solution [1,2] and limits the chemical degradation of both materials.

The chemo-mechanical behavior of cementitious materials has been estimated through previous several projects listed in the following. The first study is carried out in the laboratory on hardened cement paste (HCP), mortar or concrete. Then, field testing is performed on a massive structure to validate the laboratory results. There are very few studies which bring together these three steps, i.e., HCP, concrete in the lab and in situ experiment. The initial gap of properties (chemical and mechanical) between a material cast in a controlled laboratory environment and the *in-situ* conditions

is not often studied [3–5]. Samples cast in laboratory are generally prepared in small quantities with great care by experienced scientists in controlled environmental conditions, whereas massive concrete structures require larger batches in concrete plants in uncontrolled environmental conditions before further use by onsite workers [6]. To study durability, as illustrated by the work of Auroy & al. [7], accelerated conditioning protocols are often performed in the laboratory and compared to *in situ* natural aged samples in order to estimate how degradation develops. This technique has the advantage that it accurately represents the long-term behavior of the cementitious material [7]. However, the initial state of the aged concrete is unknown.

In the framework of the IMCB project (Impact of calcareous water on chemo-MeChanical Behaviour of concrete), which aims to understand the chemo-mechanical impact of calcareous water on the low-pH cementitious matrix, IRSN (French Institute for Radiation protection and Nuclear Safety) started a study to estimate the potential difference in results between controlled and industrial conditions. On one hand, HCP was cast in the laboratory, and on the other hand, concrete samples and massive concrete structures were cast in outside experimental platforms. After the hydration period, samples were immersed in a high volume of natural calcareous ground water. Periodic characterization was performed by SEM-EDS,  $\mu$ -CT, XRD and micro/nano-indentation. Finally, the experimental results were compared with a reactive transport model built with the HYTEC code [8].

Although a study on different low pH formulations in contact with a clay solution was conducted in the past [9], the interaction of this type of formulation has never been tested with calcareous water, suspected of being more aggressive towards the cementitious matrix than a porous clay solution (hydrolysis, carbonation, magnesium enrichment ...) and of causing not only chemical changes but also mechanical alteration.

The main objective of this paper is: i/ to study the evolution of low-pH cement matrix immersed in calcareous environment, ii/ to evaluate the gap in terms of chemistry and mechanics in degraded samples cast in different conditions.

## 2. Experimental devices

Two experimental devices were used. The first system set up in December 2018 in the IRSN underground research laboratory (URL) in Tournemire (IMCB-TR) is only composed of centimetric samples. The second one (IMCB-ODE), located in the ODE platform, is focused on macroscopic scale. In both cases, the composition of the attack solution is equivalent to natural calcareous ground water from the Cernon fault in the URL of Tournemire. Table 1 details the concentration of the main chemical elements present in this water.

Chemical element	Concentration mmol/L / pH
Ca <sup>2+</sup>	1.91
HCO <sub>3</sub> <sup>-</sup>	5.9
Mg <sup>2+</sup>	0.82
SO <sub>4</sub> <sup>2-</sup>	0.06
pH	8.2

This attack solution contains a high concentration of carbonate which, should be able to carbonate the cementitious matrix in the area in contact with the solution [9]. The low ionic strength would initiate leaching processes. Competition would occur between leaching and carbonation phenomena. The presence of magnesium in small quantities will be

considered as a tracer to follow the degradation. Indeed, due to the lack of portlandite, low-pH cementitious materials are sensitive to magnesium enrichment [10,11]

### 2.1. IMCB-TR

The first experimental device (named IMCB-TR) was installed in the URL of Tournemire (Figure 1a). The main tunnel of this URL is crossed at a specific location by the Cernon fault, which continuously discharges water from limestone aquifers located upstream.

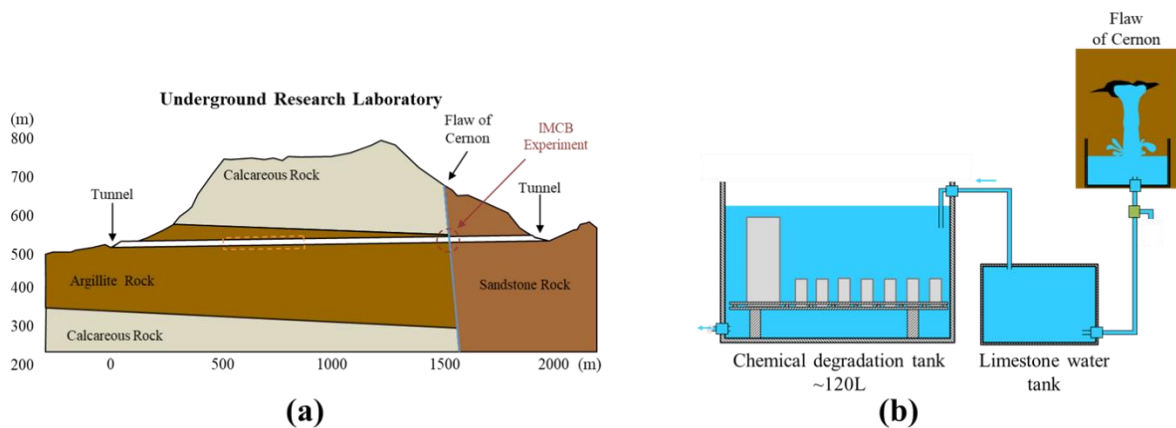


**Figure 1** Illustrative diagram (a) of the underground research laboratory of Tournemire and (b) of the IMCB-TR experimental device.

This naturally calcareous water was diverted into degradation tanks containing HCP and concrete. The samples are cylinders of three centimeters in diameter and one centimeter high. A waterproof resin (Resoltech 3030) was applied to each slice to force unidirectional diffusion. Low flow is applied in the degradation tanks to maintain continuous renewal of the solution (Figure 1b).

### 2.2. IMCB-ODE

The second in situ experimental device (named IMCB-ODE) was installed on the ODE platform of Cadarache (South of France). In October 2019, three low-pH concrete blocks 1x1x1.7m were built from a mix coming from a concrete plant.



**Figure 2** Picture of the IMCB-ODE experimental device before immersion, containing 3 low-pH concrete blocks.

A year later, a degradation tank was mounted around these blocks. 4300 liters of a synthetic solution equivalent to that from the Cernon fault was introduced into the tank (Figure 2). Acid pH regulation and salt additions were carried out weekly to ensure the stability of the solution. Sampling was carried out by coring the block and the residual hole was plugged with resin. Coring was carried out in an area far enough away from the corners of the block to assume a unidirectional attack. As the low-pH formulation changes according to the block, we assumed that, due to pH regulation and salt addition, no interaction occurred between the blocks. This paper focuses on the block cast with the low-pH formulation called T3.

### **3. Materials and methods**

#### *3.1. Raw materials*

This section describes the materials and chemical products employed in the experiments.

Low-pH formulation called T3 contain 67.5% of CEM IIIA Rombas 52.5L and 32.5% of silica fume CONDENSIL S95 DM. Sand and aggregates were calcareous from the stone quarry of Boulonnais. The aggregate on binder ratio and the sand on binder ratio were respectively equal to 2.56 and 2.27. The composition of low-pH HCP and concrete is inspired by the work of Codina & al and Bach & al [1,12]. The proportion of each constituent is detailed in table 2.

<b>Table 2</b> Composition of compounds of hardened cement paste and concrete.				
Compounds		HCP (kg/m <sup>3</sup> )	Concrete (kg/m <sup>3</sup> )	
Cement: CEM III/A 52.5L Rombas	Mineral composition (g/100g of anhydrous cement)		826	256.7
	C3S	15.9		
	C2S	2.6		
	C3A	2.4		
	C4AF	1.9		
	Slag	42.1		
	Anhydrite	4.1		
Silica Fume: CONDENSIL S95 DM		398	125	
Superplasticizer		16	6.02	
Water on cement ratio (%)		0.43	0.403	
Sand: 0/4 Boulonnais (HR: 8.3%)		0	943.3	
Aggregates 4/12 Boulonnais (HR: 1.5%)		0	980	

HCP samples of IMCB-TR were cast with deionized water in controlled laboratory conditions and kept for 2 years in a sealed bag at 20°C. The concrete samples were mixed with tap water in a concrete plant, then cast in the outside ODE platforms. A deflocculated process of silica fume was carried out before the mixing part. To replicate the sealed bag condition, concrete blocks of IMCB-ODE were wrapped with stretch film for a year. Concrete samples of IMCB-TR were kept in a sealed bag for a year in controlled laboratory conditions.

In both experiments, XRD and ATG analysis confirmed that the hydration period was long enough to remove any trace of portlandite from the cement matrix.

### 3.2. *Methods of characterization*

Every two months, a sample is extracted from IMCB-TR or IMCB-ODE. It is divided into several subsamples which are prepared differently according to the analysis for which they are intended. This section details the protocol of each analysis realized in this study.

The XRD analyses presented in this paper were carried out with an Aerie Research Edition diffractometer from Malvern-Panalytical in  $\theta-2\theta$  configuration, under  $\text{CuK}\alpha$  radiation ( $\lambda = 1.54 \text{ \AA}$ ) with a divergence slot of  $0.5^\circ$  and a rotation platform. The diffractogram profiles were performed on "solid sample" [13]. This technique aims to acquire all the crystallographic data from the degraded surface to the sound part of the cementitious material. The contact surface is first analyzed with XRD. Once the diffractogram is obtained, the sample is polished a little, then reanalyzed. This operation is repeated enough times to reach the sound part of the sample.

The  $\mu$ -CT analyses were carried out on a Brüker SkyScan 1173 equipped with a 2k pixel detector operating at 130kV and 61  $\mu\text{A}$ . The acquisition parameters are a  $0.1^\circ$  rotation pitch, a 10-averaging frame, a  $360^\circ$  rotation and a 20  $\mu\text{m}$  pixel size. Following the reconstruction, a median filter of radius 2 was applied. A K-means deconvolution [14] was

then carried out on sound concrete samples to highlight a threshold in 4 parts: aggregates, healthy matrix, a macroporous zone and pores greater than 20  $\mu\text{m}$ .

SEM-EDS analyses were carried out on carbon metallized polished sections. The acquisition was performed on SEM Hitachi S3500N with two EDS Brüker 5030 XFlash at 15 keV with x80 magnification. The pixel size is 3  $\mu\text{m}$ , at the limit of the interaction pair for this type of material [15]. The average number of photons per pixel is greater than 4000, allowing rework of signals from hyperspectral images. Post-processing was applied to concrete EDS analysis to exclude aggregates from the hyperspectral image, thus focusing only on the cementitious matrix. The intensities presented in this paper are always expressed in the intensity ratio per pixel. This implies that a pixel displaying for an element an intensity ratio of 0.2 contains 20% of this element in terms of intensity. The intensity profiles were calculated by averaging the intensity ratios in the direction parallel to the degradation front. Each point of these profiles results from the average of about 500 pixels.

The evolution of mechanical properties was estimated for HCP and concrete by micro-indentation measurements with an Anton & Paar NHT3 nano-indentor equipped with a Berkovitch tip. The tests were carried out on the same polished section as that used for the SEM-EDS analysis. Experiments were force-controlled in quasi-static mode according to the method developed by Oliver & Pharr [16]. The maximum force was set at 200mN with a loading and unloading speed of 100 mN/s.

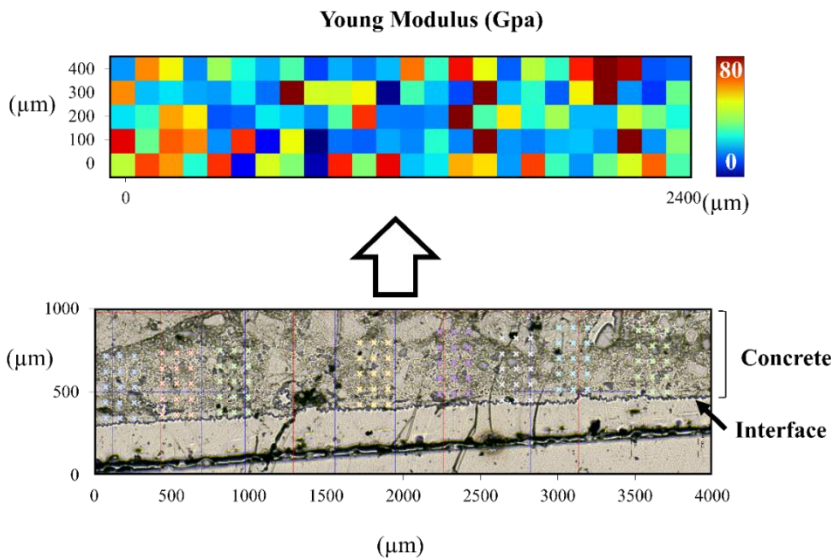


**Figure 3** Localization of the micro-indentation measurements realized on low-pH concrete immersed for 8 months in calcareous water.

As illustrated in the figure 3, 8 grids of 3x5 indents with grid spacing of 100 $\mu\text{m}$  apart were realized in the degraded zone of a concrete that had been immersed for 8 months in the IMCB-ODE. The 8 grids were then grouped together to be analysed according to the distance from the interface.

Nano-indentation maps were plotted for HCP with the same device. The grid nano-indentation technique was used to map the mechanical property distribution of the sound low-pH HCP. Tests were displacement-controlled with nanoindentation depth equal to 0.30  $\mu\text{m}$  to focus on the mechanical properties of the HCP constituents without macroscale effect [17]. Poisson's ratio was assumed to be constant and equal to 0.24. A loading and unloading speed of 12mN/s was applied for each indent. Quasi-static measurement with Olivier & Pharr technique [16,18] was performed four times on a 35 x 35 grid with grid spacing of 10  $\mu\text{m}$ .

Compressive tests were performed on concrete samples according to the NF EN 12390-13 standard, with 3 LVDT sensor strain measurements arranged at  $120^\circ$  on the lateral surface.

Porosity accessible to water was carried out by weighing the sample from saturation to dry state according to the protocol NF P 18-459 [19]. A cylindrical specimen with a diameter of 7 cm and a height of 1 cm was subjected to two consecutive steps. First, the sample is saturated with MilliQ water for 48 hours then heated at  $105^\circ\text{C}$  until constant weight is reached. The dry state of the samples is achieved when the relative mass loss between two weighs of the sample spaced 24 hours apart at  $105^\circ\text{C}$  is less than 0.05%.

#### 4. Numerical modeling

This part is dedicated to the modelling of the chemical phenomena observed in both experimental campaigns.

##### 4.1. Input and Geometry

All the calculations were performed using the reactive transport code HYTEC 4.7.4 [8]. A one-dimensional system was adopted to simulate the degradation induced by the calcareous water. The mesh used was composed of 200 rectangular sub volumes, as detailed in the figure 4. A constant boundary condition corresponding to the attack solution (Table 1) was applied on one side. Only the behaviour of the cement matrix over the first four millimeters was simulated in this model; aggregates and sand (as defined in table 2) are not considered.

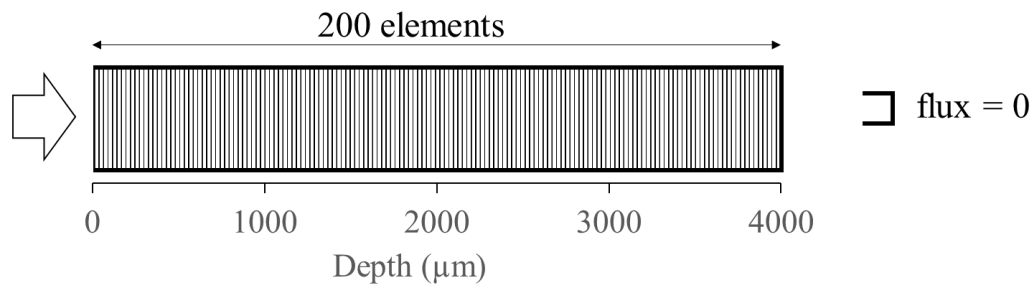


**Figure 4** Mesh and boundary conditions used for the one-dimensional chemo-transfer simulations of the cement paste specimens immersed in the calcareous solution using the reactive transport code HYTEC 4.7.4 [8].

Except for M-S-H phases, the version 1.10 of the Thermoddem thermodynamic database [20] was used in the simulations. The thermodynamic database of M-S-H was extracted from the work of Bernard & al [21]. All the phases considered during the simulation and their properties are given in the table 3.

<b>Table 3</b> Chemical, mechanical and transport properties of individual cement paste phases, taken from several sources in the literature.										
Name	Composition	Chemical properties				Mechanical properties			Transport properties	
		LogK (25 °C)	$\rho$ (kg/m <sup>3</sup> )	M (g/mol)	Ref	E (Gpa)	$\nu$	Ref	D <sub>i</sub> (m <sup>2</sup> /s)	Ref

C <sub>0.7</sub> SH	-2.8 H[+], -0.6724 H <sub>2</sub> O, 1.4 Ca[2+], 2 H <sub>4</sub> SiO <sub>4</sub>	-17.796	2291	233.4		16,4	0.24	-	4.64x10 <sup>-12</sup>	[23]
C <sub>0.8</sub> SH	-3.2 H[+], -0.218 H <sub>2</sub> O, 1.6 Ca[2+], 2 H <sub>4</sub> SiO <sub>4</sub>	-21.184	2299	249.2		16,4	0.24	-		
C <sub>0.9</sub> SH	-3.6 H[+], 1.8 Ca[2+], 2 H <sub>4</sub> SiO <sub>4</sub> , 0.1062 H <sub>2</sub> O	-25.247	2327	262.6		22,4	0.24			
C <sub>1</sub> SH	-4 H[+], 2 Ca[2+], 2 H <sub>4</sub> SiO <sub>4</sub> , 0.3978 H <sub>2</sub> O	-29.474	2358	275.52		22,4	0.24			
C <sub>1.1</sub> SH	-4.4 H[+], 2.2 Ca[2+], 2 H <sub>4</sub> SiO <sub>4</sub> , 0.7491 H <sub>2</sub> O	-33.758	2379	289.46	[22]	22,4	0.24			
C <sub>1.2</sub> SH	-4.8 H[+], 2.4 Ca[2+], 2 H <sub>4</sub> SiO <sub>4</sub> , 1.1895 H <sub>2</sub> O	-38.095	2388	305.01		22,4	0.24			
C <sub>1.3</sub> SH	-5.2 H[+], 2.6 Ca[2+], 2 H <sub>4</sub> SiO <sub>4</sub> , 1.5659 H <sub>2</sub> O	-42.473	2414	319.4		22,4	0.24			
C <sub>1.4</sub> SH	-5.6 H[+], 2.8 Ca[2+], 2 H <sub>4</sub> SiO <sub>4</sub> , 1.9144 H <sub>2</sub> O	-46.935	2447	333.29		22,4	0.24	[24]		
C <sub>1.5</sub> SH	-6 H[+], 3 Ca[2+], 2 H <sub>4</sub> SiO <sub>4</sub> , 2.2631 H <sub>2</sub> O	-51.442	2477	347.19		22,4	0.24			
C <sub>1.6</sub> SH	-6.4 H[+], 3.2 Ca[2+], 2 H <sub>4</sub> SiO <sub>4</sub> , 2.6128 H <sub>2</sub> O	-55.989	2506	361.1		22,4	0.24			
Portlandite	-2 H[+], 1 Ca[2+], 2 H <sub>2</sub> O	-22.812	2241	74.09		42,3	0.324		0	[26]
Vaterite	-1 H[+], 1 HCO <sub>3</sub> [-], 1 Ca[2+]	-2.427	2659	100.09	[25]	79,6	0.314			
Ettringite	-12 H[+], 2 Al[3+], 6 Ca[2+], 3 SO <sub>4</sub> [2-], 38 H <sub>2</sub> O	-57.009	1767	1255.11	[27]	22.4	0.25			
Hydrotalcite	-14 H[+], 2 Al[3+], 4 Mg[2+], 17 H <sub>2</sub> O	-73.757	1949	443.33	[28]	30.2	0.3	[29]		
Unreacted SiO <sub>2</sub>	1 H <sub>4</sub> SiO <sub>4</sub> , -2 H <sub>2</sub> O	2.714	2072	60		79.6	0.314	[30]		
SiO <sub>2</sub> (am)	1 H <sub>4</sub> SiO <sub>4</sub> , -2 H <sub>2</sub> O	2.714	2072	60		4.3	0.24	[31]		
MSH-078	0.78 Mg[2+], 1 H <sub>4</sub> SiO <sub>4</sub> , 0.26 H <sub>2</sub> O, -1.56 H[+]	-7.25	2300	128.8		8.6	0.24			
MSH-083	0.83 Mg[2+], 1 H <sub>4</sub> SiO <sub>4</sub> , 0.33 H <sub>2</sub> O, -1.66 H[+]	-7.90	2300	138		8.6	0.24			
MSH-100	1 Mg[2+], 1 H <sub>4</sub> SiO <sub>4</sub> , 0.6 H <sub>2</sub> O, -2 H[+]	-10.43	2300	161	[21]	8.6	0.24	[32]		
MSH-130	1.30 Mg[2+], 1 H <sub>4</sub> SiO <sub>4</sub> , 2.1 H <sub>2</sub> O, -2.6 H[+]	-14.96	2300	165.6		8.6	0.24			
MC005SH-078	0.78 Mg[2+], 0.05 Ca[2+], 1 H <sub>4</sub> SiO <sub>4</sub> , 0.33 H <sub>2</sub> O, ...	-7.92	2300	131.1		8.6	0.24			
KatoiteSi1	-12 H[+], 2 Al[3+], 3 Ca[2+], 1 H <sub>4</sub> SiO <sub>4</sub> , 8 H <sub>2</sub> O	-71.168	2843	402.34	[33]	22.4	0.25	[24]		
Aqueous	-	-	-	-	-	0	0	-	2x10 <sup>-9</sup>	[34]
Aggregates	-1 H[+], 1 HCO <sub>3</sub> [-], 1 Ca[2+]	-	2660	-		79.6	0.314		0	[26]
Sand	-1 H[+], 1 HCO <sub>3</sub> [-], 1 Ca[2+]	-	2670	-		79.6	0.314	[24]	0	[26]

A limit of the approach proposed in this paper concerns the coexistence of silica fume (unreacted SiO<sub>2</sub>) and amorphous silicon (SiO<sub>2</sub>(am)). Both species have the same chemical behavior but with different mechanical properties [30,31]. Due to convergence issues, it has not been possible to make calculations with both species, only amorphous silicon was considered in simulations. This choice would impact the homogenized mechanical properties within element of the mesh.

#### 4.2. Chemical modelling

The coupling between chemistry and transport is provided by the following equation in pure diffusion:

$$\frac{\partial \omega c_i}{\partial t} = \nabla \cdot (D_e(\omega) \nabla c_i) - \frac{\partial \omega \underline{c}_i}{\partial t} \quad (1)$$

Where  $D_e$  represents the effective diffusion coefficient,  $\omega$  is the material porosity,  $c_i$  and  $\underline{c}_i$  represent mobile species  $i$  concentration in solution and the concentration fixed in solid phases, respectively. The B-dot activity correction model was applied in this study.

The porosity  $\omega$  may evolve during the simulation, depending on the precipitations of species. The consequences for the effective diffusion coefficient  $D_e$  are calculated from the modified version of Archie's law:

$$D_e(\omega) = D_e(\omega_0) \left( \frac{\omega - \omega_c}{\omega_0 - \omega_c} \right)^\alpha \quad (2)$$

Where  $\alpha$  is an empirical coefficient equal to 2 in this study [35],  $\omega_0$  is the initial porosity and  $\omega_c$  is a threshold below which diffusion stops.

As proposed by Dormieux & al [36], the initial effective diffusion coefficient  $D_e$  of the cement matrix can be estimated from the proportions of different phases with the following equation:

$$D_e(\omega_0) = D_{csh} \left( \frac{1 + 2 \sum_i \varphi_i \frac{D_i - D_{csh}}{D_i + 2 \cdot D_{csh}}}{1 - \sum_i \varphi_i \frac{D_i - D_{csh}}{D_i + 2 \cdot D_{csh}}} \right)^\alpha \quad (3)$$

Where  $\varphi_i$ ,  $D_i$  are respectively the volume ratio and the diffusion coefficient of the phase I and  $D_{csh}$  is the coefficient of diffusion of C-S-H species. Only capillary porosity and C-S-H are considered as diffusive phases [26,31,34,37]. In agreement with the work of Ulm & al [38] the porosity in the C-S-H phases is equal to 28%. This value is calculated using a thermodynamic calculation, based on table 3, that assumes the dissolution of all anhydrous phases.

#### 4.3. Mechanical modelling

To estimate the evolution of mechanical properties in the cement matrix, a classical analytical homogenization technique was applied, which is particularly appropriate here since the material exhibits matrix-inclusion type morphology [39]. The chosen approach involved utilizing the Mori-Tanaka scheme [40] to estimate the mechanical properties of the degraded cement matrix. It is worth noting that such this scheme has been previously employed to estimate properties of cement-based materials in various contexts [31,37,41]. The continuous reference matrix considered in this study is the CS-H matrix.

To estimate the evolution of mechanical properties in the cement matrix, a classical analytical homogenization technique was applied, which is particularly appropriate here since the material exhibits a matrix-inclusion type morphology [37]. The chosen approach involved utilizing the Mori-Tanaka scheme [40] to estimate the mechanical properties of the degraded cement matrix. It is worth noting that this scheme has been previously employed to estimate properties of cement-based materials in various contexts [30,35,39]. The continuous reference matrix considered in this study is the CS-H matrix.

The shear and compressibility coefficients of the equivalent homogenized material ( $k_{homo}^{est}$  and  $g_{homo}^{est}$ , respectively) are given by:

$$k_{HCP}^{MT} = \frac{k_{C-S-H} + \frac{4g_{csh}}{3} \sum_{i=1}^{N^{ph}} f_i \frac{k_i - k_{csh}}{k_i + \frac{4}{3}g_{csh}}}{1 - \sum_{i=1}^{N^{ph}} f_i \frac{k_i - k_{csh}}{k_i + \frac{4}{3}g_{csh}}} \quad (4)$$

$$g_{HCP}^{MT} = \frac{g_{csh} + H_{csh} \sum_{i=1}^{N^{ph}} f_i \frac{g_i - g_{csh}}{g_i + H_{csh}}}{1 - \sum_{i=1}^{N^{ph}} f_i \frac{g_i - g_{csh}}{g_i + H_{csh}}} \quad (5)$$

Where  $N^{ph}$  is the number of phases,  $k_{C-S-H}$  and  $g_{C-S-H}$  the shear and compressibility coefficients of C-S-H,  $k_i$  and  $g_i$  the shear and compressibility coefficients of the phase  $i$ ,  $f_i$  the volume fraction of the phase  $i$ , and  $H_{C-S-H}$  is the following term:

$$H_{csh} = \frac{g_{csh}(\frac{3}{2}k_{csh} + \frac{4}{3}g_{csh})}{(k_{csh} + 2g_{csh})} \quad (6)$$

The corresponding values of macroscopic Young's modulus  $E_{HCP}^{MT}$  and Poisson's ratio  $\nu_{HCP}^{MT}$  can be calculated from:

$$E_{HCP}^{MT} = \frac{9k_{HCP}^{MT} g_{HCP}^{MT}}{3k_{HCP}^{MT} + g_{HCP}^{MT}} \quad (7)$$

$$v_{HCP}^{MT} = \frac{3k_{HCP}^{MT} - 2g_{HCP}^{MT}}{6k_{HCP}^{MT} + 2g_{HCP}^{MT}} \quad (8)$$

## 5. Results

### 5.1. Initial Pore network

The total porosity accessible to water estimated, according to NF P 18-459 protocol, on molded samples are respectively 30% for the HCP and 12 % for the concrete. These results are considered as the initial value of the total porosity in IMCB-TR.

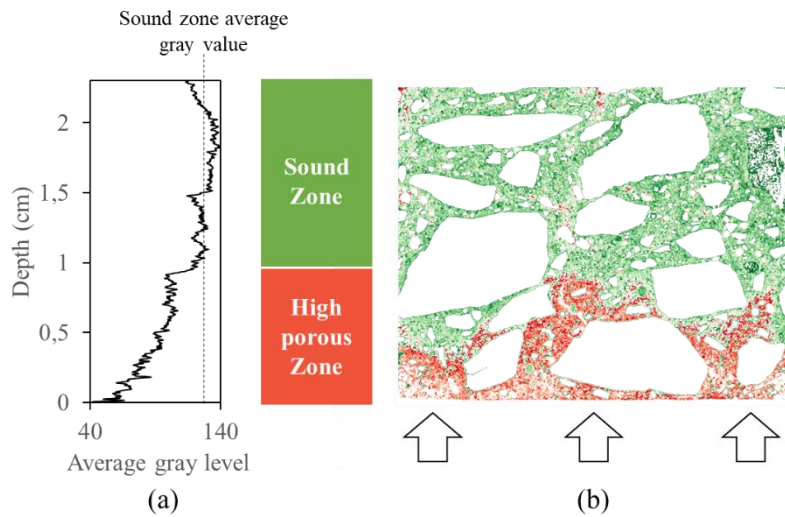


**Figure 5** (a) Evolution of average gray value and (b) segmentation in two clusters depending on gray value of sound low-pH concrete blocks before installation in IMCB-ODE.

The fluctuation of gray value in  $\mu$ CT analysis is related to the evolution of density. Figure 5 illustrates the presence of a skin effect in the concrete block of IMCB-ODE. The zone with high porosity covers almost 1 cm of depth. This phenomenon is likely due to a drying phenomenon during the hydration process despite the protective film.

### 5.2. Hydration modelling

The initial volume proportions of each mineral were calculated using the geochemical module of HYTEC (CHESS 3.13.4) coupled with the thermodynamic database presented in table 3. As previously observed in a prior study [9], we assume that the remaining clinker and slag phases can be considered negligible. The chemical solver had access to the complete database, except for the Afm phases. As no Afm species were detected through XRD analysis, katoite was

chosen instead of monosulfoaluminate or monocarbaluminates based on a previous study on low-pH formulation [42]. The porosity (total and capillary) was calculated by subtracting the mass of hydrates from the initial mass of raw materials.

The proportions of all anhydrous phases in g/l were input into the chemical solver for both the hydrated cement paste (HCP) and the concrete, allowing for the estimation of hydration products. Subsequently, a calculation was conducted using the concrete results to determine the characteristics of the cement matrix in the absence of aggregates and sand, referred to as the Equivalent HCP. Simulations of degradation in the concrete were performed using the Equivalent HCP. The results of the hydration calculation are presented in table 4.

Sample	C0.8SH		Katoite	Ettringite	Unreacted SiO <sub>2</sub>	Aqueous		Aggregates	Sand
	Dry	Saturated				Total	Capillary		
HCP	0.40	0.56	0.11	0.11	0.08	0.30	0.14	-	-
Concrete	0.12	0.16	0.02	0.02	0.03	0.12	0.07	0.36	0.33
Equivalent HCP	0.38	0.53	0.08	0.06	0.09	0.39	0.24	-	-

We assume that this approach only provides an estimation of the full hydration. However, after a year of hydration the main chemical processes occurred in a low-pH cement matrix [43,44].

Based on the equation (3), the coefficient of diffusion of each formulation was calculated by considering the distribution of species proposed in the table 4. The effective coefficients of diffusion of the HCP and Equivalent HCP were respectively  $4.5 \times 10^{-12}$  m<sup>2</sup>/s and  $6.8 \times 10^{-12}$  m<sup>2</sup>/s. To simulate the high porous zone observed in the concrete of IMCB-ODE (Figure 5), a coefficient of diffusion of  $2 \times 10^{-10}$  m<sup>2</sup>/s was applied to Equivalent HCP.

### 5.3. Mineralogical evolution

Figure 6 summarizes the distribution of the average intensity ratios of silicon, sulfur, calcium, and magnesium from the surface to the sound zone of the sample for all cementitious materials studied in this paper, at 2, 4, 8 and 24 months.

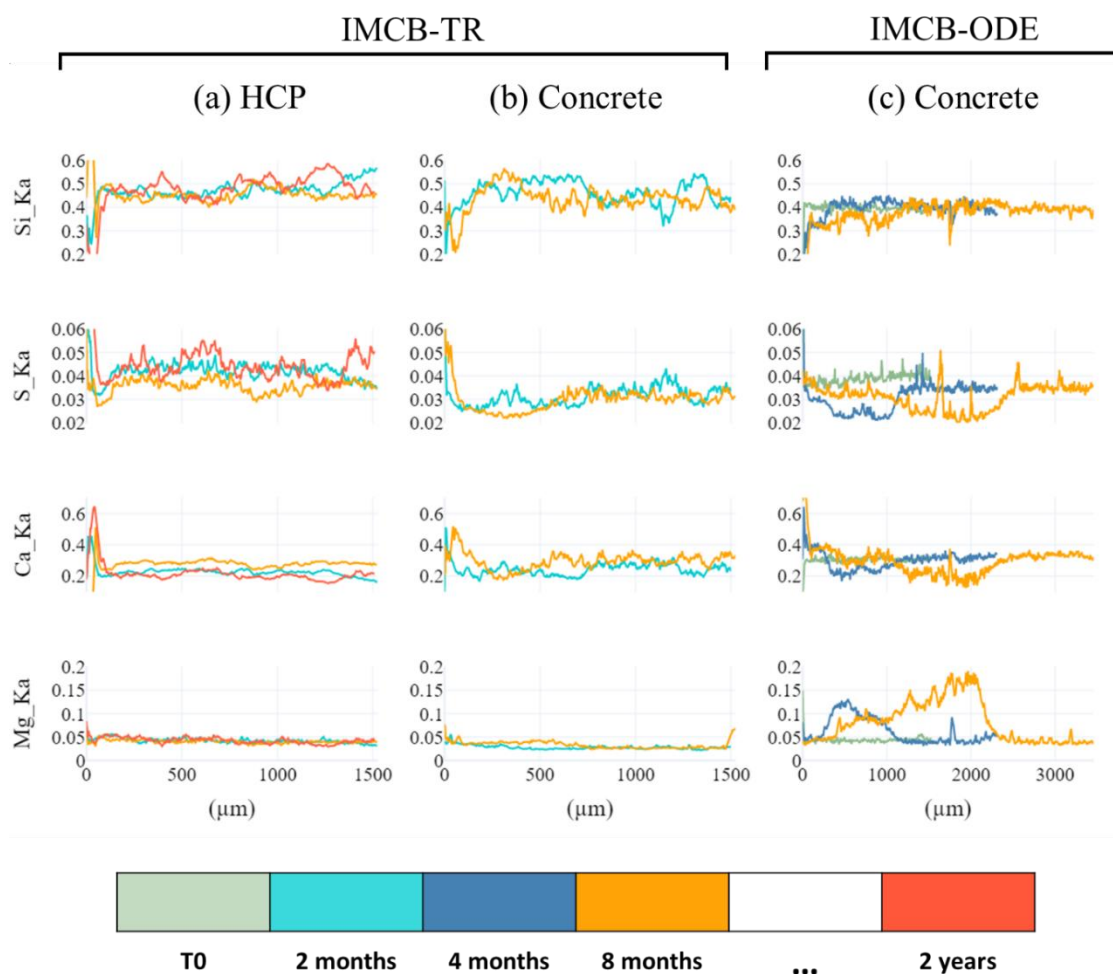


**Figure 6** SEM-EDS analysis of the evolution of the Ka line intensity ratio of silicon, sulfur, calcium and magnesium in a hardened cement paste (a) and in two concretes (b) and (c), immersed for up to two years in IMCB-TR and IMCB-ODE.

The monitoring of the intensity ratio of these four elements allows an estimation of the mineralogical changes occurring in the cement matrix. The decrease in sulfur intensity is characteristic of a dissolution of ettringite. The sound zone appears when the signal rises. In this study, a change in calcium intensity may mean either calcium carbonate precipitation or C-S-H decalcification. Finally, a significant increase in magnesium intensity is related to magnesium enrichment.

Whatever experimental time was considered, the HCP of IMCB-TR does not seem to be impacted by the degradation solution. A peak is observable at the interface on the calcium intensity, suggesting the presence of a calcium carbonate layer. The concrete of IMCB-TR shows a more marked chemical response. At 4 months, the sulfur intensity ratio profile shows an alteration zone up to 600  $\mu\text{m}$  deep. This alteration may be subdivided in two parts. The first 200  $\mu\text{m}$  are rich in calcium, suggesting the precipitation of calcium carbonate, while the next 400  $\mu\text{m}$  are the site of magnesium enrichment.

The same mechanisms are even more markedly present in the concrete of the IMCB-ODE. The ratio of intensity for magnesium reaches 20% at 8 months. Between 4 and 8 months, a magnesium-enriched layer moves to the core of the sample, followed by a calcium enrichment zone.

Figure 7 shows SEM-EDS analysis composed with elementary maps of the intensity ratio of calcium and magnesium. This characterization was carried out on the IMCB-ODE concrete after 8 and 19 months immersed in the IMCB-ODE device.

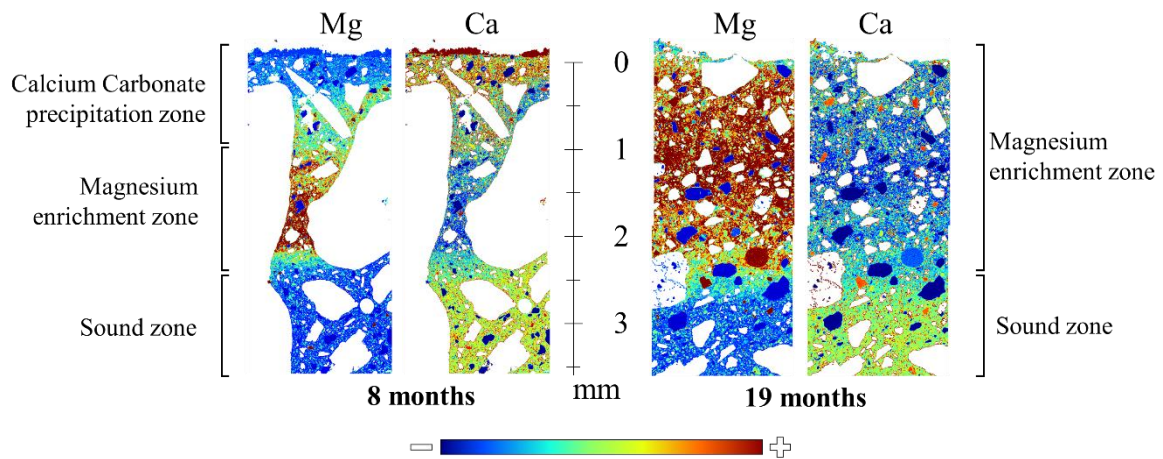


**Figure 7** SEM-EDS analysis of a low-pH T3 concrete immersed for 8 months and 19 months in IMCB-ODE. This analysis includes magnesium and calcium elemental maps.

At 8 months, in the first millimeter a calcium enrichment is visible on the elemental maps, followed by magnesium enrichment. The sound material is observed 3 millimeters from the surface. Referring to the work of Dauzères & al [9] on the aqueous carbonation of low-pH matrices, the calcium enrichment zone can reasonably be considered to be related to the precipitation of calcium carbonate and C-S-H decalcification within the cementitious matrix. The two enrichments (calcium and magnesium) do not coexist, which implies that the chemical stability domains of these two zones are not compatible.

At 19 months, large magnesium enrichment is noticed from the surface to 3 millimeters deeper. Upstream of this enrichment, no calcium carbonate precipitate is detected, unlike at 8 months. A hypothesis to explain the lack of calcium enrichment may be flaking of the calcium carbonate precipitates due to loss of cohesiveness with the cement matrix. Indeed, as illustrated by the figure 8 at 10 days, cracking was several times observed between the cement matrix and the calcium carbonate layer. The split likely appears during the sample preparation. It only happens for samples 8 to 12 months old, before the layer is in contact with the cement matrix; afterwards it disappears.

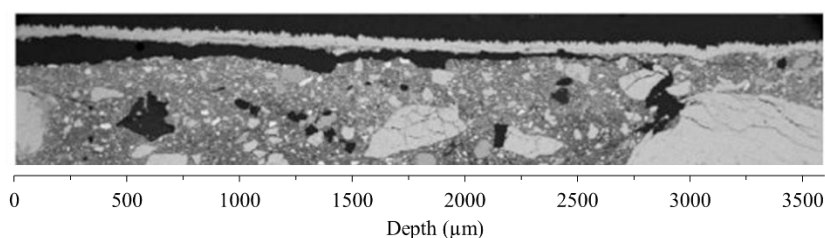


**Figure 8** SEM-BSE analysis of a low-pH T3 concrete immersed for 10 months in IMCB-ODE. Focus on the layer of calcium carbonate at the surface.

As previously observed in the figure 6 and confirmed by figure 9, the HCP-TR does not undergo the same degradation mechanisms. After 4 years of degradation, the EDS analysis (figure 9c) reveals no magnesium enrichment. A layer of calcium carbonate has precipitated at 200  $\mu\text{m}$  from the surface, within the cement matrix. Both BSE analyses (figure 9a and b) show a difference in gray level of the cement matrix located on each side of the layer. This change suggests an alteration of the cement matrix close to the interface. A hypothesis could be that, in the degraded part, new precipitations occurred with the same chemical elements, which does not affect the EDS spectrum. For instance, no change in the EDS spectrum would happen through the precipitation of amorphous silicon with calcium carbonates instead of C-S-H.

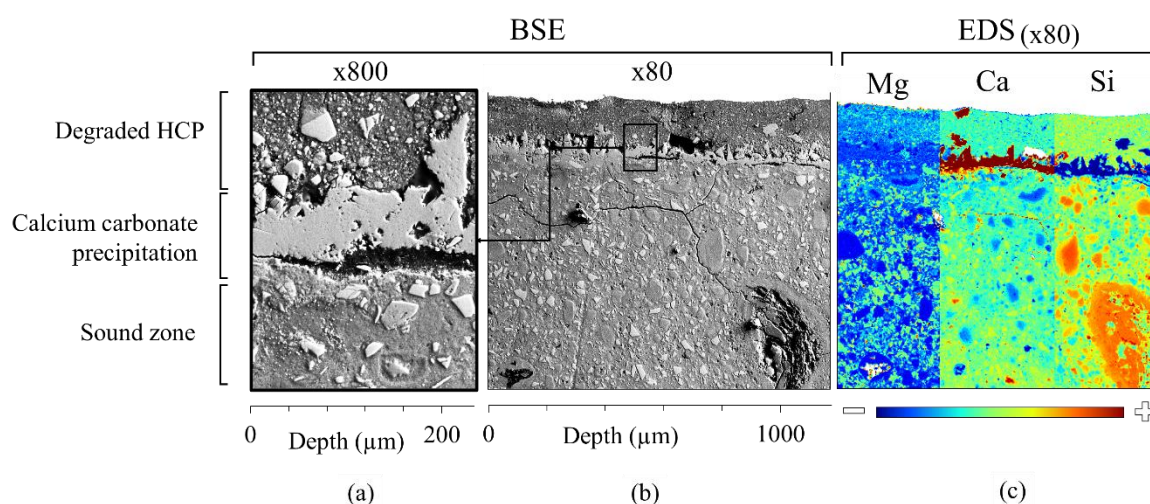


**Figure 9** SEM-EDS analysis of HCP immersed for 4 years in IMCB-TR. (a) BSE at x800 magnification, (b) BSE at x80 magnification and (c) EDS elemental mapping of intensity ratio of Mg, Ca, Si at x80 magnification.

Unfortunately, XRD analysis is not possible in this zone due to the low mechanical strength of the contact with the calcium carbonate layer. Indeed, the degraded HCP zone is not continuous throughout the surface of the polished section. A solid XRD analysis of the surface would be interfered with by the partial presence of the calcium carbonate layer.

Despite the effort made during the sample preparation to force unidirectional degradation, a heterogeneity in terms of the degradation front is observed in the SEM-EDS analysis. Figure 10 shows the magnesium enrichment measured by SEM-EDS of two zones located on the same polished section containing concrete which was immersed for 4 months

in IMCB-ODE. Figure 10a corresponds to profiles of the average intensity ratio of magnesium in the first 2 mm for both zones. In figure 10b and c, a threshold was applied on the EDS elemental map of magnesium to only conserve pixels where the intensity ratio is higher than 5% for the magnesium and 90% for the calcium, in order to highlight magnesium enrichment and calcium carbonate precipitation.

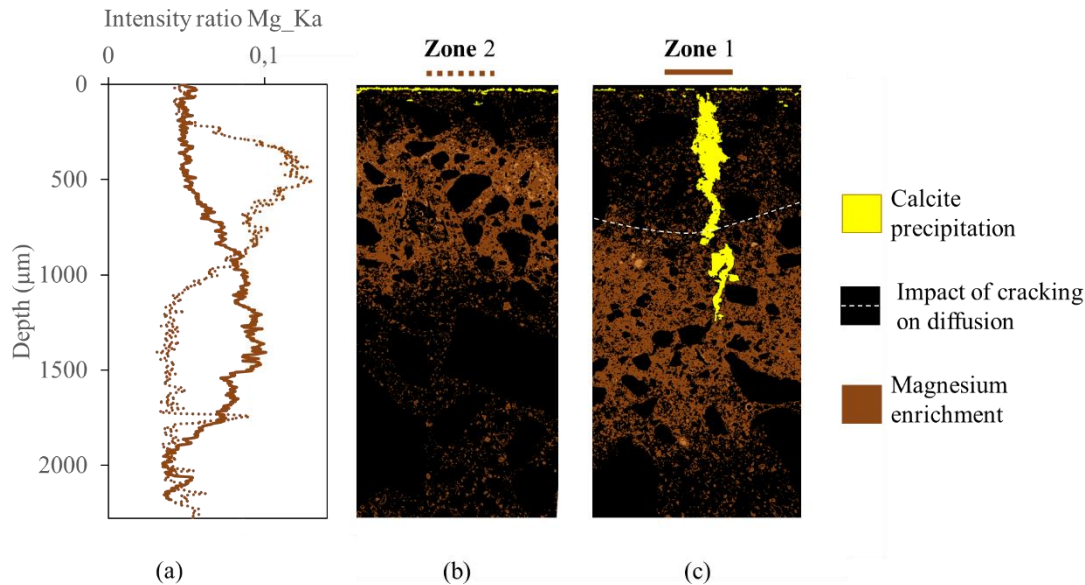


**Figure 10** SEM-EDS analysis of magnesium enrichment and calcium carbonate precipitates in two zones of a low-pH T3 concrete immersed for 4 months in IMCB-ODE. (a) This analysis includes two phase recognitions and a curve showing the evolution of the intensity ratio of the Ka line of magnesium in the two analyzed zones.

In zone 1 (Figure 10c), the precipitation of calcium carbonate in the crack and the difference of localization of magnesium enrichment, compared to zone 2 (Figure 10b), suggest the presence of the crack before the immersion in IMCB-ODE. As illustrated by the dotted line on figure 10c, due to the cracking the diffusion in this zone cannot be considered as unidirectional. The diffusion was significantly accelerated, leading to magnesium enrichment with an offset equal to 1 mm compared to zone 2 (Figure 10a).

To determine the mineralogical suite versus depth, XRD analysis was carried out on HCP and concrete after 8 months of immersion in IMCB-TR (Figure 11 and Figure 12). Detecting the degradation state by XRD becomes challenging in low pH HCP due to the absence of Portlandite. In this study, ettringite was considered as an indicator of the degradation state. Duchesne et al. [45] and other researchers have explained that in solutions with low aluminum and sulfate content, ettringite is the dissolved mineral that follows the dissolution of Portlandite. Therefore, the dissolution of ettringite in the cement matrix occurs through the diffusion of calcareous water in the pore network. Figure 11 is a focus of XRD diffractograms made around the peak at  $9.1^\circ$  (in  $2\theta$ ) characterizing the presence of ettringite. Both cementitious materials studied in figure 11 underwent 8 months of immersion in IMCB-TR.

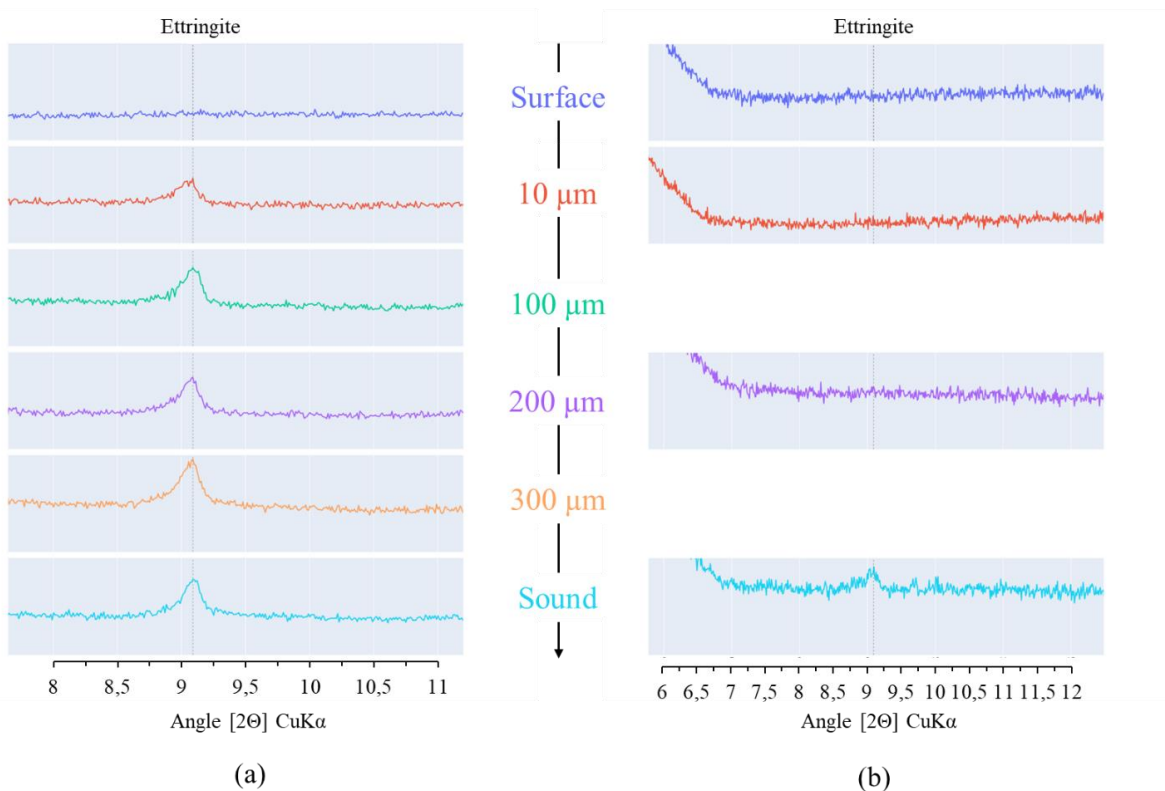


**Figure 11** Part of X-ray diffractogram profiles focusing on the main peak of ettringite of (a) a low-pH T3 cement paste and (b) a low-pH T3 concrete, both immersed for 8 months in IMCB-TR.

At 10 microns from the interface, the ettringite signal is already visible in the HCP, which confirms that this cementitious material is only altered on the surface. On the contrary, in concrete, at 200 microns from the interface, ettringite is still not visible. Unlike HCP, concrete immersed in IMCB-TR is subject to degradation.

Figure 12 focuses on the presence of vaterite in concrete immersed for 8 months in IMCB-TR, a calcium carbonate produced from the decalcification of C-S-H [46,47].

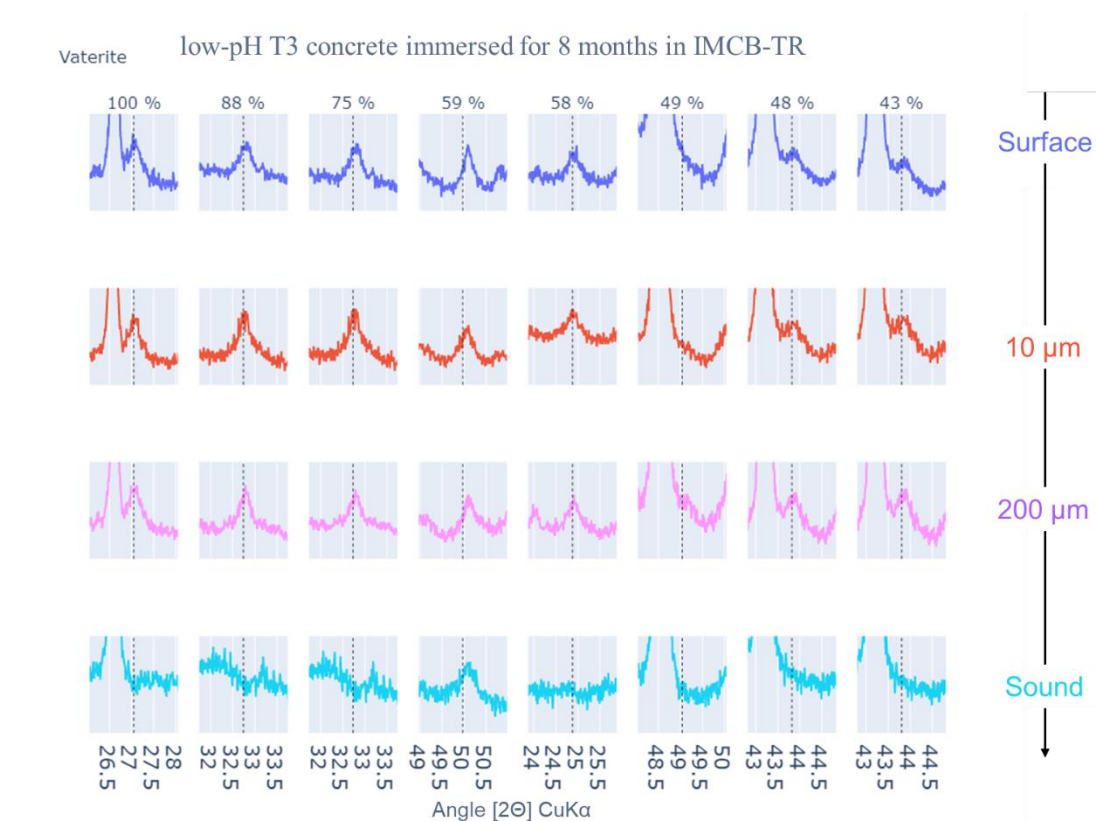


**Figure 12** Part of X-ray diffractogram profiles focusing on the main peak of vaterite of low-pH T3 concrete immersed for 8 months in IMCB-TR.

The XRD analysis proves the presence of vaterite in the first 200 microns of the analyzed sample. By making the hypothesis that the main source of calcium for the precipitation of calcium carbonates is the C-S-H, vaterite is considered in this paper as the only possibility of calcium carbonate precipitation.

#### 5.4. Mechanical evolution

This section describes the results of nano-micro indentation measurements. The first part is dedicated to the study of the sound cement matrix, in which different techniques are compared at different scales. Nano and micro indentation measurements were performed on low-pH HCP. In parallel, compressive tests were carried out on concrete to estimate the Young's modulus.

Blue and Orange histograms of the figure 13a correspond respectively to the distribution of 5158 nano indents and 385 micro indents. It's interesting to note a similarity of Young's modulus distribution at nano and macro scale. As detailed by previous studies [17,48], due to the nanometric size of the penetration depth, nano-indentation provides an estimate of the mechanical properties of the cement paste, without taking into account the capillary pore. Regarding the hydration calculation in table 4, the capillary pores account for a volume ratio of 14% in the HCP. Apart from this macro-porosity, the HCP consists of C-S-H, unreacted silica fume, ettringite, and katoite. To be consistent with the hydration calculation of table 4, no distinction was made between C-S-H Low Density and C-S-H High Density. Besides, the selected Afm phases and ettringite have theoretically the same mechanical properties [26]. Thus, only three clusters were considered for the deconvolution steps of nano-indentation results. Figure 13b and c illustrate the

results of the deconvolution. The main detected cluster is located at a mean of 16.3 GPa with a weight of 57%. The second cluster is located at 25.51 with a weight of 28%. The last one covers the values from 40 to 80 GPa with a weight equal to 13%. After a comparison with the hydration calculation of Table 4, a name was assigned to each cluster corresponding to the potential phases included in it. Indeed, C-S-H should theoretically constitute 65%, katoite with ettringite 26% and the unreacted silica fume 9% of the solid part of the cement matrix.

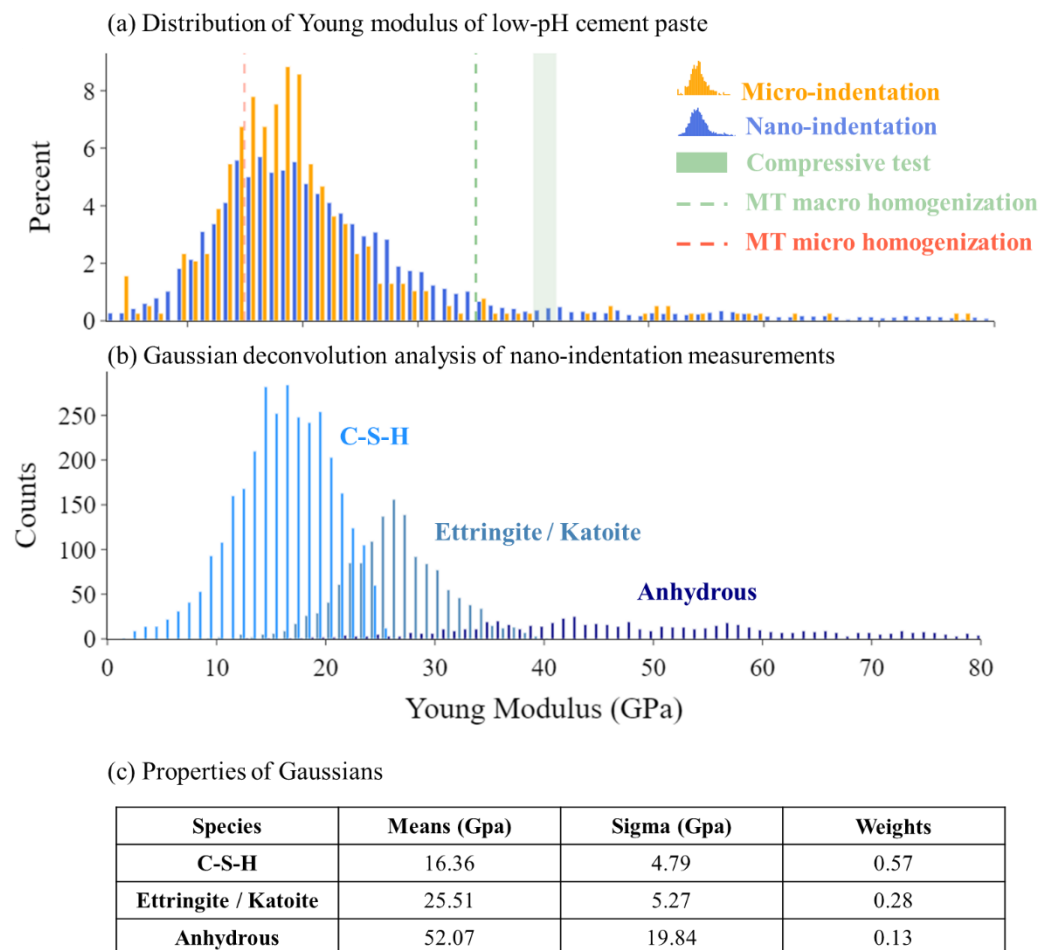


**Figure 13** (a) Distribution of Young's modulus in sound low-pH T3 HCP performed with different techniques (nanoindentation, micro-indentation, compressive test), (b) Gaussian deconvolution of nano-indentation measurements and (c) Properties of Gaussian deconvolution.

A question remains about the Young's modulus estimated for the C-S-H phase. Studies realized on Portland HCP highlight a Young's modulus of C-S-H Low-Density around 22 GPa  $\pm$  6 GPa and C-S-H High Density around 31 GPa  $\pm$  3 GPa [17,38,48,49]. All these works were performed on C-S-H with a high calcium to silicon atomic ratio (Ca/Si ratio) close to 1.6. In the low-pH cement matrix, C-S-H has a low Ca/Si ratio equal to 0.8. The low-pH cementitious matrix maintains a macroscopic Young's modulus similar to that of Portland HCP [1,12]. The lack of portlandite is compensated by a low capillary pore. The mechanical properties of C-S-H should be close to those of Portland cement. Due to the absence of knowledge about this topic, the value obtained in the figure 13c was used in the model for the C-S-H with Ca/Si ratio equal to 0.8 and 0.7.

As illustrated in the figure 13b, a homogenized Young's modulus of the HCP was calculated using the mineralogical composition from table 4 and the mechanical properties from table 3, resulting in a value of 14.3 GPa. Similarly, applying the same approach to the concrete yielded a Young's modulus of 35 GPa. In both cases, the homogenized Young's modulus is lower than the measured value (18 GPa for the HCP and 40 GPa for the concrete). However, the difference is still within an acceptable range considering the assumptions made throughout the calculation process.

Figure 14 details the distribution of Young's modulus in the calcium-enriched zone of a concrete immersed 8 months in IMCB-ODE (Figure 7). Whatever the distance considered from the interface, the median value is always close to 20 GPa. A few points are located below 10 GPa; these are threshold values between a healthy matrix and a decalcified matrix [50].

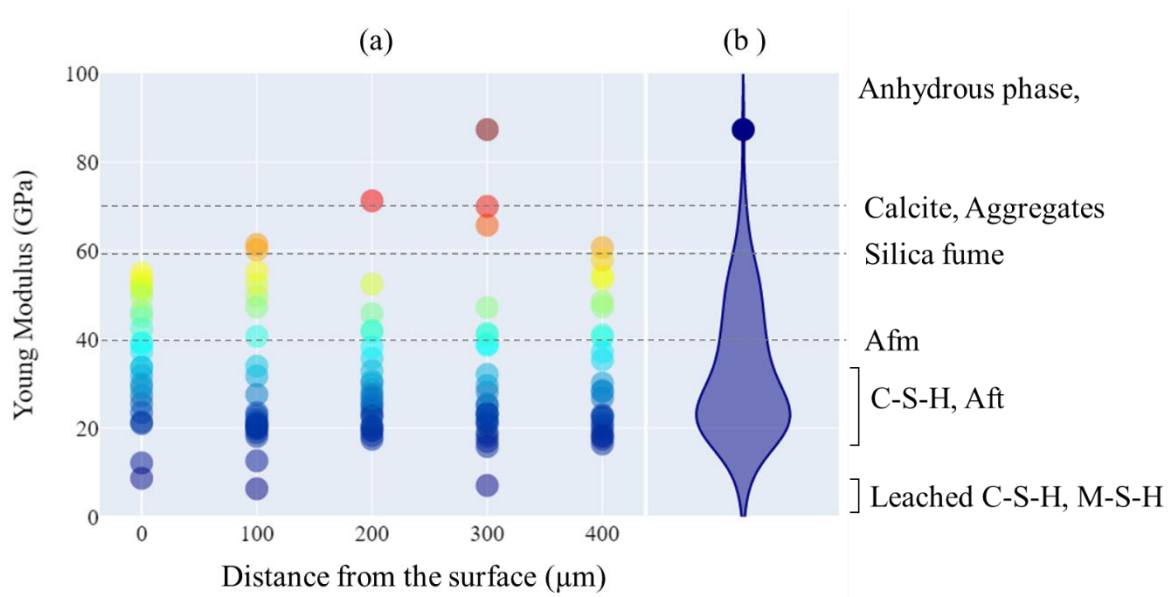


**Figure 14** (a) Distribution of Young's moduli measured by micro-indentation as a function of depth and (b) global violin diagram for a low-pH T3 concrete immersed for 8 months in IMCB-ODE.

According to the figure 14b, the average Young's modulus is equal to 21 GPa. The micro-indentation measurement provides an estimation of the macroscopic Young's modulus including the capillary pores. Considering the initial high porosity of this zone (Figure 5), the relatively high macroscopic Young's modulus suggests the precipitation of species with high Young's modulus such as vaterite (Table 3).

### 1.1. Chemo-mechanical modelling

Figure 15 and figure 16 present the results of the three chemo-transport simulations carried out with the model described above. The first one (Figure 15 I) aims to simulate the chemo-mechanical evolution of HCP cast in laboratory-controlled conditions and immersed in Cernon water (Table 1). In the second one (Figure 15 II), all the inputs are characteristic of a concrete made in laboratory-controlled conditions, then immersed in Cernon water (Table 1). Finally, the last one (Figure 15 III) focuses on the behavior of the high porous zone observed in the concrete immersed in IMCB-ODE. The degradation time is equal to 8 months, in all simulations.

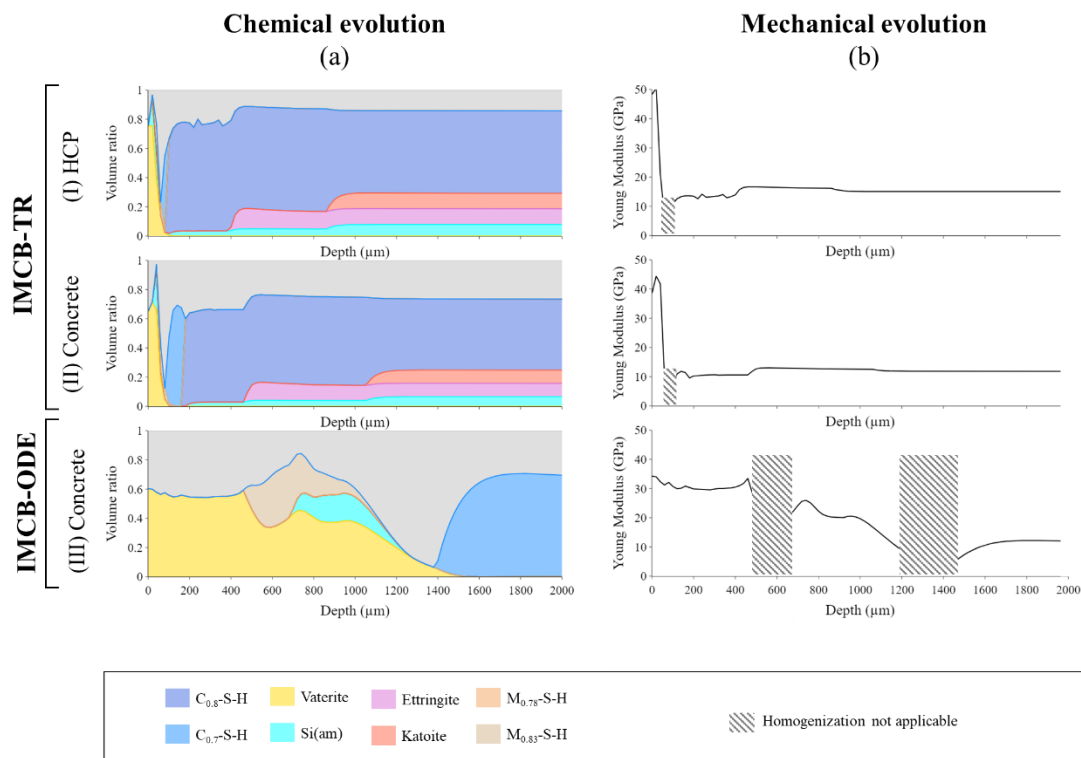


**Figure 15** Model of (a) mineralogical and (b) mechanical evolution of low-pH T3 concrete immersed for 8 months in Cernon water.

Porosity closing is observed in the HCP after 8 months of immersion (Figure 15 Ia and Figure 16 I) due to the presence of a layer of vaterite combined with a small amount of amorphous silicon and M-S-H precipitations at the surface. Two M-S-H phases precipitate in this model, with a magnesium to silicon ratio (Mg/Si ratio) of 0.78 and 0.83 (Figure 16 I). Before the closing, the chemical attack dissolved ettringite over the first 500  $\mu\text{m}$  and katoite over 1 mm. Incipient C-S-H decalcification is observed in favor of C-S-H with Ca/Si ratio equal to 0.7. Except in the vaterite precipitation zone where the homogenized Young's modulus reaches 50 GPa, the impact on the mechanical properties is low (Figure 15 Ib). Contrary to the model, the dissolution depth of ettringite is detected 10  $\mu\text{m}$  below the surface at 8 months (Figure 11). Except for that point, the simulation globally agrees with the experimental results (Figure 6). The model cannot precipitate a vaterite layer in the cement matrix, as observed in Figure 9. This phenomenon requires mechanical modelling to simulate the flaking of the first layer of vaterite at the surface.

In the figure 15 IIa, the same mechanisms are observed, with a delay due to the higher initial porosity. Compared to the previous simulation, the quantity of amorphous silicon increases, whereas the maximum volume ratio of the vaterite layer decreases. The concentration of M-S-H is constant and located in the same zone as the amorphous silicon precipitation. Only M-S-H with Mg/Si ratio equal to 0.83 is observed in this model (Figure 16 II). As observed in Figure 16 I, the porosity closing is a consequence of the precipitation of vaterite, M-S-H and amorphous silicon in the same zone. Due to the lack of information about transport properties of M-S-H, the model considers this amorphous species as a potential barrier to diffusion. It's interesting to note that the vaterite layer tends to thicken. The area impacted by the decalcification of C-S-H is larger, likely due to the delays of porosity closing. Conversely, ettringite and katoite do not evolve significantly between the two simulations (Figure 15 Ia and Figure 15 IIa). As illustrated by Figure 6, concrete immersed in IMCB-TR follows the same overall trend as HCP.

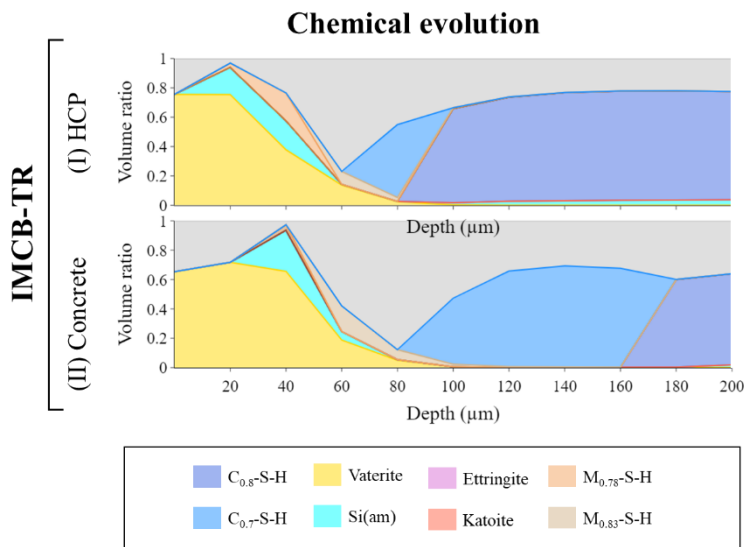


**Figure 16** Simulation focusing on the first 200  $\mu\text{m}$  of mineralogical evolution of low-pH T3 HCP and concrete immersed for 8 months in calcareous water.

The model in the figure 15 IIIa shows different behaviour of the concrete immersed for 8 months in IMCB-ODE. The high coefficient of diffusion simulating the high porous zone (Figure 5) changes the mineralogical evolution without porosity closing. The first 500  $\mu\text{m}$  are only composed of 60% of vaterite and 40% porosity. The end of the first zone corresponds to the beginning of M-S-H precipitation, which continues to a depth of 1200  $\mu\text{m}$ . In this zone, vaterite decreases from 60% to 20%. Amorphous silicon appears between 700  $\mu\text{m}$  and 1200  $\mu\text{m}$ . The magnesium enrichment reaches 20% at its maximum value. From 1000  $\mu\text{m}$ , the proportion of M-S-H and amorphous silicon decreases down to 1400  $\mu\text{m}$ . From this depth, the volume ratio of C-S-H with Ca/Si ratio of 0.7 increases. 2000  $\mu\text{m}$  deeper, the cement matrix is only composed of 68% decalcified C-S-H and 32% capillary pores. The mechanical consequence of these mineralogical changes is an increase of Young's modulus in the first zone, caused by the massive vaterite precipitation. The homogenization scheme estimated a stable Young's modulus close to 30 GPa in this part of the sample. The increase agrees with the micro-indentation measurements of figure 14. However, the calculated value is higher than the experimental result. The reason can be attributed to the lack of amorphous silicon in this zone. The SEM-EDS analysis of the figure 6 shows an intensity ratio of silicon equal to 30%, which suggests the presence of amorphous silicon cohabitating with the vaterite. The low Young's modulus of this species would appear to decrease the homogenized Young's modulus. As explained previously, the approach proposed in this paper does not consider the feedback from mechanics in the chemical model. Thus, the potential flaking noticed in Figure 7b cannot be studied.

Overall, the model proposed in this section follows degradation scenarios observed experimentally at 8 months. HPC and concrete immersed in IMCB-TR undergo porosity closure, which limits the alteration of the cement matrix. On the other hand, calcium enrichment corresponding to vaterite precipitation happened in the concrete immersed in IMCB-ODE. Upstream of this enrichment, a zone composed of M-S-H, amorphous silicon and vaterite is noticed.

## 2. Discussion

**What is the chemo-mechanical response of a low-pH cementitious matrix immersed in limestone water containing low concentration of magnesium?**

All the results presented in this paper seem to point the degradation scenario towards the formation of two enrichment zones, one in calcium at the interface and another further upstream in magnesium (Figure 17).

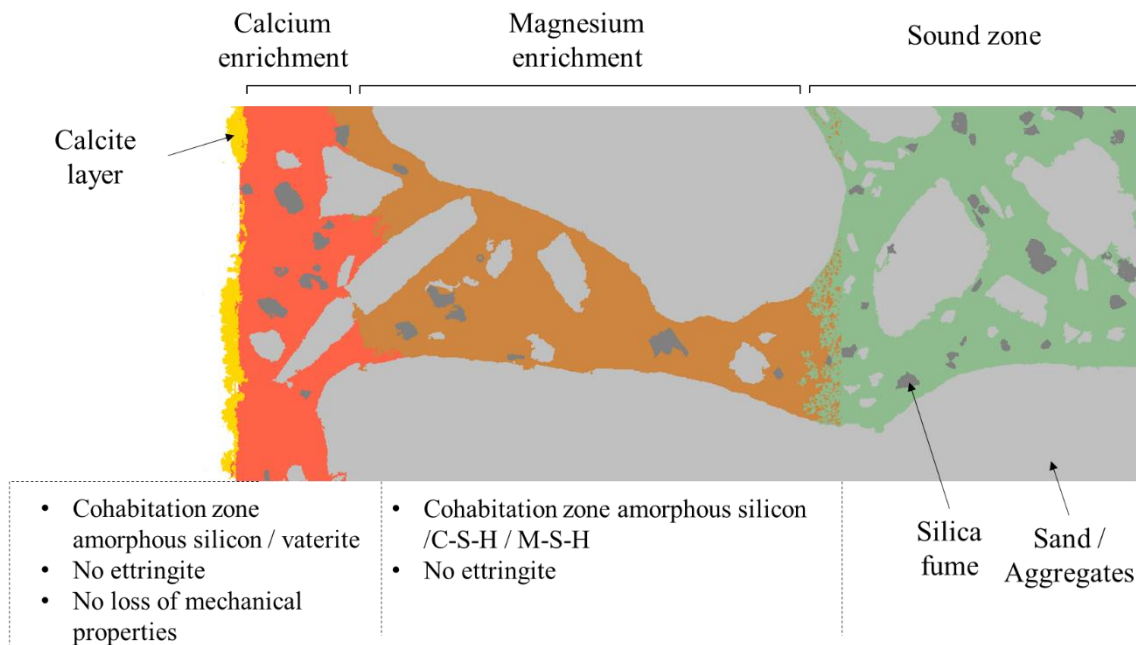


**Figure 17** Illustrative diagram of the degradation scenario proposed to explain the alteration of low-pH cementitious matrix in contact with Cernon water.

The only study dealing with aqueous carbonation of low-pH cementitious materials was published by Dautères & al in 2014 [9]. In this paper, one of the consequences of aqueous carbonation is the precipitation of calcite within the matrix as observed for the vaterite in this study. The divergence about the type of polymorph of calcium carbonate is likely due to experiment conditions. First, the low-pH formulation used in the work of Dautères & al [9] contained fly ash, which may participate in the carbonation process [51–53]. Secondly, the tests were performed with a fugacity representative of underground conditions. The fugacity has an impact on thermodynamic equilibrium constants. In lab conditions, Kangni-Foli & al. [47] detected, in unsaturated conditions, vaterite as the main calcium carbonate product of C-S-H carbonation. Mechanically, as illustrated by the figure 14 and figure 15, the calcium enrichment tends to locally increase the Young's modulus of the degraded zone [54]. The reason is related to the high mechanical properties of calcium carbonates. However, this zone also seems to be brittle, likely due to the presence of amorphous silicon. Indeed, figure 7 and figure 8 suggest a flaking phenomenon in the calcium enrichment zone.

Despite the low concentration of magnesium in the attack solution, magnesium enrichment occurred in the cement matrix. The M-S-H phases, shown in figure 17, were not clearly identified in this study. However, numerically no brucite or hydrotalcite precipitate was evidenced (Figure 15). This result agrees with the work of Bernard & al [11,21,55]. Displacement and enlargement of the magnesium-enriched strip is noticed over time (Figure 6 and Figure 7).

**What is the influence of the connected poral network on the degradation scenario?**

The experimental campaign and the numerical simulation highlight the large influence of the total porosity on the degradation scenario.

When the total porosity is lower than 40%, the carbonation process tends to close the porosity (Figure 15). The calcium-enriched strip protects the cement matrix from the chemical attack. A small quantity of magnesium species and amorphous silicon is nevertheless observed (Figure 16 and Figure 6). Numerical results show that the closing phenomenon is induced by the combination of precipitation of calcium carbonate, M-S-H and amorphous silicon. Despite the porosity closing, diffusion of carbonate still occurred slowly, leading to the precipitation of the vaterite strip within the matrix (Figure 9). The degraded cementitious materials located between this strip and the surface of the materials are likely composed of amorphous silicon and calcium carbonate.

In the case of a high porous cementitious material with micro-cracking, carbonation cannot have an impact on the porosity closing. The degradation of the cementitious materials is initiated by the formation of two enrichment zones, one in calcium at the interface and another further upstream in magnesium (Figure 7a). A flaking mechanism occurred in the calcium enrichment zone (Figure 7a). The magnesium enrichment increases versus time (Figure 7a).

### **Are the tests carried out on cement paste in a controlled environment representative of the actual conditions experienced by the concrete?**

Overall, the present study proves that results obtained on HPC are transposable to concrete. The cement paste was manufactured in the laboratory in a controlled environment, scrupulously following the spoiling protocol. Concretes were mixed at the ITER concrete plant and then brought to the platform ODE via a spinning top truck. The cure period before IMCB-TR was carried out in a waterproof bag at 20 ° C for 2 years. At the surface, the total porosity is 10 % lower in the HCP but it does not impact the chemo-mechanical behavior of the cement matrix subjected to attack solution (Figure 6a and Figure 6b).

The concrete of IMCB-ODE underwent a different conservation protocol, which induced the appearance of a macro-porous zone of one centimeter depth from the interface. This skin effect drastically increased the transport properties of the material, which did not just accelerate degradation. A different degradation scenario is followed, in which large calcium and magnesium enrichment is observed. The low mechanical properties of the M-S-H phases, [32] combined with the flaking phenomenon suspected in the calcium enrichment zone, raise some questions about the macroscopic mechanical behaviour of the degraded zone. However, the alteration would be limited to the macro-porous zone, which does not jeopardize the integrity of the concrete structure.

### **3. Conclusion**

In conclusion, this study aimed to provide insights into the chemo-mechanical behavior of a low-pH cementitious matrix in contact with calcareous ground water. The experimental campaign, along with numerical simulations, revealed some mineralogical changes within the matrix:

- At the interface, a visible layer of calcium carbonate formed.
- The first hundred microns exhibited calcium enrichment and the presence of amorphous silica. Vaterite, identified in this area, contributed to a higher Young's modulus. A suspected flaking phenomenon in this zone was attributed to the low Young's modulus of amorphous silicon.
- Upstream, magnesium enrichment was observed, with concentrations reaching up to 20% of the material's volume ratio. The low mechanical properties of magnesian phases raised concerns about the durability of this zone.

Additionally, the study aimed to estimate the potential deviation of results between controlled laboratory conditions and uncontrolled industrial conditions. The conservation protocol significantly influenced the chemical response of the

cementitious materials. Large concrete blocks cured outside and wrapped with stretch film exhibited a high porous zone at the interface, altering the transport properties and degradation scenario. In contrast, cementitious materials cured in controlled conditions showed a tendency to form a layer of calcium carbonates, closing the porosity and preventing degradation in the cement matrix. After immersion, the high porous zone exhibited two enrichment zones, one in calcium at the interface and another further upstream in magnesium. These zones raise concerns about potential flaking in the calcium carbonate zone and the low Young's modulus of the magnesium phases. However, it appears that these observed changes are limited to the high porous zone and do not significantly impact the integrity of the concrete structure.

Continuing the experiments for a minimum of 3 years is anticipated to provide further insights and validate hypotheses made in this study, particularly regarding the flaking phenomenon. The precipitation of the vaterite layer within the material in the HCP after 4 years of immersion raises some questions about the fate of the degraded part located downstream. Improvements to the designed model are necessary to deepen our understanding, including integrating mechanics feedback on chemical evolution and studying the consequences of the absence of amorphous silicon in the calcium enrichment zone. Additionally, implementing the coexistence of amorphous silica and silica fume is crucial for accurate modeling of the evolution of mechanical properties in the cement matrix.

In summary, this study sheds light on the chemo-mechanical behavior of low-pH cementitious matrices, highlighting key mineralogical changes and the influence of conservation protocols on the chemical response and degradation scenarios. The insights gained will contribute to further research and understanding in the field of cementitious materials.

#### 4. Acknowledgements

This study was realized in the framework of the international consortium ODOBA and the European project EURAD-MAGIC. The authors would like to express their special appreciation and thanks to teams of ODE platforms for the time spent on our experimental devices.

#### 5. References

- [1] M. Codina, C. Cau-dit-Coumes, P. Le Bescop, J. Verdier, J.P. Ollivier, Design and characterization of low-heat and low-alkalinity cements, *Cement and Concrete Research*. 38 (2008) 437–448. <https://doi.org/10.1016/j.cemconres.2007.12.002>.
- [2] T.T.H. Bach, C.C.D. Coumes, I. Pochard, C. Mercier, B. Revel, A. Nonat, Influence of temperature on the hydration products of low pH cements, *Cement and Concrete Research*. 42 (2012) 805–817. <https://doi.org/10.1016/j.cemconres.2012.03.009>.
- [3] S. Poyet, B. Bary, E. Coppens, Analysis of water transport in unsaturated conditions: Comparison between labcrete and fieldcrete, *Construction and Building Materials*. 205 (2019) 443–455. <https://doi.org/10.1016/j.conbuildmat.2019.02.034>.
- [4] V. Baroghel-Bouny, M. Dierkens, X. Wang, A. Soive, M. Saillio, M. Thiery, B. Thauvin, Ageing and durability of concrete in lab and in field conditions: investigation of chloride penetration, *Journal of Sustainable Cement-Based Materials*. 2 (2013) 67–110. <https://doi.org/10.1080/21650373.2013.797938>.
- [5] B.A. Suprenant, Dealing with the ‘labcrete-realcrete’ gap, *Concr. Prod.* January. (1998) 37–618.
- [6] R.J. Torrent, *Service Life Prediction: Theorecrete, Labcrete and Realcrete Approaches*, (n.d.).

- [7] M. Auroy, S. Poyet, P. Le Bescop, J.-M. Torrenti, T. Charpentier, M. Moskura, X. Bourbon, Impact of carbonation on unsaturated water transport properties of cement-based materials, *Cement and Concrete Research*. 74 (2015) 44–58. <https://doi.org/10.1016/j.cemconres.2015.04.002>.
- [8] J. van der Lee, L. De Windt, V. Lagneau, P. Goblet, Module-oriented modeling of reactive transport with HYTEC, *Computers & Geosciences*. 29 (2003) 265–275. [https://doi.org/10.1016/S0098-3004\(03\)00004-9](https://doi.org/10.1016/S0098-3004(03)00004-9).
- [9] A. Dauzères, P. Le Bescop, C. Cau-Dit-Coumes, F. Brunet, X. Bourbon, J. Timonen, M. Voutilainen, L. Chomat, P. Sardini, On the physico-chemical evolution of low-pH and CEM I cement pastes interacting with Callovo-Oxfordian pore water under its in situ CO<sub>2</sub> partial pressure, *Cement and Concrete Research*. 58 (2014) 76–88. <https://doi.org/10.1016/j.cemconres.2014.01.010>.
- [10] A. Dauzères, G. Achiedo, D. Nied, E. Bernard, S. Alahrache, B. Lothenbach, Magnesium perturbation in low-pH concretes placed in clayey environment—solid characterizations and modeling, *Cement and Concrete Research*. 79 (2016) 137–150. <https://doi.org/10.1016/j.cemconres.2015.09.002>.
- [11] E. Bernard, B. Lothenbach, F. Le Goff, I. Pochard, A. Dauzères, Effect of magnesium on calcium silicate hydrate (C-S-H), *Cement and Concrete Research*. 97 (2017) 61–72. <https://doi.org/10.1016/j.cemconres.2017.03.012>.
- [12] T. Bach, I. Pochard, C. Cau-Dit-Coumes, C. Mercier, A. Nonat, Prediction of long-term chemical evolution of a low-pH cement designed for underground radioactive waste repositories, in: *Cement-Based Materials for Nuclear Waste Storage*, 2013: pp. 239–249. [https://doi.org/10.1007/978-1-4614-3445-0\\_21](https://doi.org/10.1007/978-1-4614-3445-0_21).
- [13] D. Planel, J. Sercombe, P. Le Bescop, F. Adenot, J.-M. Torrenti, Long-term performance of cement paste during combined calcium leaching–sulfate attack: kinetics and size effect, *Cement and Concrete Research*. 36 (2006) 137–143. <https://doi.org/10.1016/j.cemconres.2004.07.039>.
- [14] J.A. Hartigan, M.A. Wong, Algorithm AS 136: A K-Means Clustering Algorithm, *Journal of the Royal Statistical Society. Series C (Applied Statistics)*. 28 (1979) 100–108. <https://doi.org/10.2307/2346830>.
- [15] D.P. Bentz, P.E. Stutzman, C. Haecker, S. Remond, SEM/X-Ray Imaging of Cement-Based Materials, (1999). <https://www.nist.gov/publications/semx-ray-imaging-cement-based-materials> (accessed July 22, 2021).
- [16] G.M. Pharr, W.C. Oliver, Measurement of Thin Film Mechanical Properties Using Nanoindentation, *MRS Bulletin*. 17 (1992) 28–33. <https://doi.org/10.1557/S0883769400041634>.
- [17] C. Hu, Z. Li, A review on the mechanical properties of cement-based materials measured by nanoindentation, *Construction and Building Materials*. 90 (2015) 80–90. <https://doi.org/10.1016/j.conbuildmat.2015.05.008>.
- [18] W.C. Oliver, G.M. Pharr, Measurement of hardness and elastic modulus by instrumented indentation: Advances in understanding and refinements to methodology, *Journal of Materials Research*. 19 (2004) 3–20. <https://doi.org/10.1557/jmr.2004.19.1.3>.
- [19] P. NF, P 18-459: Essai pour béton durci-Essai de porosité et de masse volumique, AFNor (Association Française de Normalisation). [In French] Paris: AFNor. (2010).
- [20] Ph. Blanc, A. Lassin, P. Piantone, M. Azaroual, N. Jacquemet, A. Fabbri, E.C. Gaucher, Thermoddem: A geochemical database focused on low temperature water/rock interactions and waste materials, *Applied Geochemistry*. 27 (2012) 2107–2116. <https://doi.org/10.1016/j.apgeochem.2012.06.002>.
- [21] E. Bernard, B. Lothenbach, C. Cau-Dit-Coumes, C. Chlique, A. Dauzères, I. Pochard, Magnesium and calcium silicate hydrates, Part I: Investigation of the possible magnesium incorporation in calcium silicate hydrate (C-S-H) and of the calcium in magnesium silicate hydrate (M-S-H), *Applied Geochemistry*. 89 (2018) 229–242. <https://doi.org/10.1016/j.apgeochem.2017.12.005>.
- [22] C. Roosz, P. Vieillard, P. Blanc, S. Gaboreau, H. Gailhanou, D. Braithwaite, V. Montouillout, R. Denoyel, P. Henocq, B. Madé, Thermodynamic properties of C-S-H, C-A-S-H and M-S-H phases: Results from direct measurements and predictive modelling, *Applied Geochemistry*. 92 (2018) 140–156. <https://doi.org/10.1016/j.apgeochem.2018.03.004>.

- [23] N. Venkovic, L. Sorelli, B. Sudret, T. Yalams, R. Gagné, Uncertainty propagation of a multiscale poromechanics-hydration model for poroelastic properties of cement paste at early-age, *Probabilistic Engineering Mechanics*. 32 (2013) 5–20.
- [24] C.-J. Haecker, E.J. Garboczi, J.W. Bullard, R.B. Bohn, Z. Sun, S.P. Shah, T. Voigt, Modeling the linear elastic properties of Portland cement paste, *Cement and Concrete Research*. 35 (2005) 1948–1960. <https://doi.org/10.1016/j.cemconres.2005.05.001>.
- [25] R.A. Robie, H. BS, Thermodynamic properties of minerals and related substances at 298.15° K and 1 bar (105 pascals) pressure and at higher temperatures., (1978).
- [26] F. Péalès, Y. Monerie, A. Socié, Effects of the microstructural uncertainties on the poroelastic and the diffusive properties of mortar, *Journal of Theoretical, Computational and Applied Mechanics*. (2022). <https://doi.org/10.46298/jtcam.8849>.
- [27] H.A. Berman, E.S. Newman, Heat of formation of calcium aluminate monosulfate at 25 C, *Journal of Research of the National Bureau of Standards. Section A, Physics and Chemistry*. 67 (1963) 1.
- [28] H.F.W. Taylor, *Cement Chemistry*, Thomas Telford, 1997.
- [29] X.-Z. Zhou, Z.-Y. Han, J.-J. Zheng, Z.-Y. Zheng, Y.-X. Zhang, X.-H. Zhang, A multi-step scheme for evaluating the elastic moduli of partially leached cement paste, *Construction and Building Materials*. 344 (2022) 128095. <https://doi.org/10.1016/j.conbuildmat.2022.128095>.
- [30] C. Hu, Z. Li, Property investigation of individual phases in cementitious composites containing silica fume and fly ash, *Cement and Concrete Composites*. 57 (2015) 17–26. <https://doi.org/10.1016/j.cemconcomp.2014.11.011>.
- [31] E. Stora, B. Bary, Q.-C. He, E. Deville, P. Montarnal, Modelling and simulations of the chemo–mechanical behaviour of leached cement-based materials: Leaching process and induced loss of stiffness, *Cement and Concrete Research*. 39 (2009) 763–772. <https://doi.org/10.1016/j.cemconres.2009.05.010>.
- [32] C. Dewitte, A. Bertron, M. Neji, L. Lacarrière, A. Dauzères, Chemical and Microstructural Properties of Designed Cohesive M-S-H Pastes, *Materials*. 15 (2022) 547. <https://doi.org/10.3390/ma15020547>.
- [33] P. Blanc, X. Bourbon, A. Lassin, E.C. Gaucher, Chemical model for cement-based materials: Temperature dependence of thermodynamic functions for nanocrystalline and crystalline C–S–H phases, *Cement and Concrete Research*. 40 (2010) 851–866.
- [34] M. Bogdan, Morphological multiscale modeling of cementitious materials–Application to effective diffusive properties prediction, PhD Thesis, École normale supérieure de Cachan-ENS Cachan, 2015.
- [35] L. De Windt, P. Devillers, Modeling the degradation of Portland cement pastes by biogenic organic acids, *Cement and Concrete Research*. 40 (2010) 1165–1174. <https://doi.org/10.1016/j.cemconres.2010.03.005>.
- [36] L. Dormieux, K. Djimedo, F.-J. Ulm, *Mircoporomechanics*, Wiley, 2006.
- [37] B. Bary, Simplified coupled chemo-mechanical modeling of cement pastes behavior subjected to combined leaching and external sulfate attack, *International Journal for Numerical and Analytical Methods in Geomechanics*. 32 (2008) 1791–1816. <https://doi.org/10.1002/nag.696>.
- [38] G. Constantinides, F.-J. Ulm, The nanogranular nature of C–S–H, *Journal of the Mechanics and Physics of Solids*. 55 (2007) 64–90. <https://doi.org/10.1016/j.jmps.2006.06.003>.
- [39] J.D. Eshelby, The Continuum Theory of Lattice Defects, in: F. Seitz, D. Turnbull (Eds.), *Solid State Physics*, Academic Press, 1956: pp. 79–144. [https://doi.org/10.1016/S0081-1947\(08\)60132-0](https://doi.org/10.1016/S0081-1947(08)60132-0).
- [40] T. Mori, K. Tanaka, Average stress in matrix and average elastic energy of materials with misfitting inclusions, *Acta Metallurgica*. 21 (1973) 571–574. [https://doi.org/10.1016/0001-6160\(73\)90064-3](https://doi.org/10.1016/0001-6160(73)90064-3).

- [41] V. Nežerka, V. Hrbek, Z. Prošek, M. Somr, P. Tesárek, J. Fládr, Micromechanical characterization and modeling of cement pastes containing waste marble powder, *Journal of Cleaner Production*. 195 (2018) 1081–1090. <https://doi.org/10.1016/j.jclepro.2018.05.284>.
- [42] M. Neji, A. Dauzères, A. Grellier, J. Sammaljärvi, O. Tikkanen, M. Siitari-Kauppi, Comparison of the chemo-mechanical behavior of low-pH cement exposed to calcareous water and to argillite pore water, *Applied Geochemistry*. (2022) 105392. <https://doi.org/10.1016/j.apgeochem.2022.105392>.
- [43] B. Lothenbach, D. Rentsch, E. Wieland, Hydration of a silica fume blended low-alkali shotcrete cement, *Physics and Chemistry of the Earth, Parts A/B/C*. 70–71 (2014) 3–16. <https://doi.org/10.1016/j.pce.2013.09.007>.
- [44] B. Lothenbach, G. Le Saout, M. Ben Haha, R. Figi, E. Wieland, Hydration of a low-alkali CEM III/B–SiO<sub>2</sub> cement (LAC), *Cement and Concrete Research*. 42 (2012) 410–423. <https://doi.org/10.1016/j.cemconres.2011.11.008>.
- [45] J. Duchesne, A. Bertron, Leaching of Cementitious Materials by Pure Water and Strong Acids (HCl and HNO<sub>3</sub>), in: M. Alexander, A. Bertron, N. De Belie (Eds.), *Performance of Cement-Based Materials in Aggressive Aqueous Environments: State-of-the-Art Report*, RILEM TC 211 - PAE, Springer Netherlands, Dordrecht, 2013: pp. 91–112. [https://doi.org/10.1007/978-94-007-5413-3\\_4](https://doi.org/10.1007/978-94-007-5413-3_4).
- [46] J. Li, Q. Yu, H. Huang, S. Yin, Effects of Ca/Si Ratio, Aluminum and Magnesium on the Carbonation Behavior of Calcium Silicate Hydrate, *Materials*. 12 (2019) 1268. <https://doi.org/10.3390/ma12081268>.
- [47] E. Kangni-Foli, S. Poyet, P. Le Bescop, T. Charpentier, F. Bernachy-Barbé, A. Dauzères, E. L'Hôpital, J.-B. d'Espinose de Lacaillerie, Carbonation of model cement pastes: The mineralogical origin of microstructural changes and shrinkage, *Cement and Concrete Research*. 144 (2021) 106446. <https://doi.org/10.1016/j.cemconres.2021.106446>.
- [48] M. Vandamme, F.-J. Ulm, Nanoindentation investigation of creep properties of calcium silicate hydrates, *Cement and Concrete Research*. 52 (2013) 38–52. <https://doi.org/10.1016/j.cemconres.2013.05.006>.
- [49] H.M. Jennings, J.J. Thomas, J.S. Gevrenov, G. Constantinides, F.-J. Ulm, A multi-technique investigation of the nanoporosity of cement paste, *Cement and Concrete Research*. 37 (2007) 329–336. <https://doi.org/10.1016/j.cemconres.2006.03.021>.
- [50] G. Constantinides, F.-J. Ulm, The effect of two types of C-S-H on the elasticity of cement-based materials: Results from nanoindentation and micromechanical modeling, *Cement and Concrete Research*. 34 (2004) 67–80. [https://doi.org/10.1016/S0008-8846\(03\)00230-8](https://doi.org/10.1016/S0008-8846(03)00230-8).
- [51] T. Chen, M. Bai, X. Gao, Carbonation curing of cement mortars incorporating carbonated fly ash for performance improvement and CO<sub>2</sub> sequestration, *Journal of CO<sub>2</sub> Utilization*. 51 (2021) 101633. <https://doi.org/10.1016/j.jcou.2021.101633>.
- [52] R. Kurda, J. de Brito, J.D. Silvestre, Carbonation of concrete made with high amount of fly ash and recycled concrete aggregates for utilization of CO<sub>2</sub>, *Journal of CO<sub>2</sub> Utilization*. 29 (2019) 12–19. <https://doi.org/10.1016/j.jcou.2018.11.004>.
- [53] D. Zhang, Q. Yang, M. Mao, J. Li, Carbonation performance of concrete with fly ash as fine aggregate after stress damage and high temperature exposure, *Construction and Building Materials*. 242 (2020) 118125. <https://doi.org/10.1016/j.conbuildmat.2020.118125>.
- [54] J.M. Chi, R. Huang, C.C. Yang, Effects of carbonation on mechanical properties and durability of concrete using accelerated testing method, *Journal of Marine Science and Technology*. 10 (2002) 7.
- [55] E. Bernard, A. Dauzères, B. Lothenbach, Magnesium and calcium silicate hydrates, Part II: Mg-exchange at the interface “low-pH” cement and magnesium environment studied in a C-S-H and M-S-H model system, *Applied Geochemistry*. 89 (2018) 210–218. <https://doi.org/10.1016/j.apgeochem.2017.12.006>.